

Liquid Metal-Tailored PEDOT:PSS for Noncontact Flexible Electronics with High Spatial Resolution

Bin Chen, Mingying Wu, Shenwen Fang, Yudong Cao, Liyuan Pei, Haibin Zhong, Chang Sun, Xianglong Lin, Xuanyang Li, Jianfeng Shen,* and Mingxin Ye*



Cite This: <https://doi.org/10.1021/acsnano.2c08760>



Read Online

ACCESS |



Metrics & More



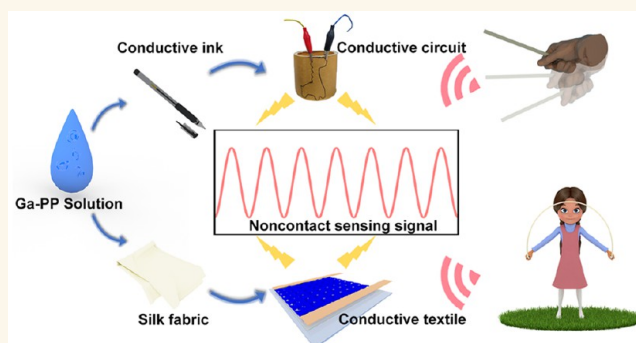
Article Recommendations



Supporting Information

ABSTRACT: Electric field-based noncontact flexible electronics (EF-NFEs) allow people to communicate with intelligent devices through noncontact human–machine interactions, but current EF-NFEs with limited detections (usually <20 cm) distance often lack a high spatial resolution. Here, we report a versatile material for preparing EF-NFE devices with a high spatial resolution to realize everyday human activity detection. Eutectic gallium–indium alloy (EGaIn) was introduced into poly(3,4-ethylenedioxythiophene):poly(styrenesulfonate) (PEDOT:PSS) chains to fabricate this material, named Ga-PP. The introduction of EGaIn successfully regulates the intra- and interchain interactions of PEDOT chains and thus increases the π -electron accumulation on Ga-PP chains, which facilitates improvement of the electron storage of Ga-PP and its noncontact sensing ability. The water solubility of the obtained Ga-PP can reach approximately 15 mg/mL, comparable to that of commercial PEDOT:PSS, thus making Ga-PP suitable for various design strategies to prepare EF-NFE devices. We demonstrate that a conductive textile with a noncontact sensing ability can be achieved by immersing a commercial silk fabric into a Ga-PP solution for 5 min. With a detection distance exceeding 1 m, the prepared Ga-PP-based conductive textile (Ga-PP-CT) possesses outstanding noncontact sensing sensitivity, showing advantages in tracing the locations of signal sources and distinguishing motion states. Surprisingly, even when placed in water, Ga-PP-CT can be used to monitor the movement signals of athletes in different sporting events and output specific noncontact response signals for different sports. Intriguingly, the Ga-PP solution itself can be used to construct noncontact sensing conductive circuits, displaying the potential to be incorporated into smart electronics.

KEYWORDS: liquid metal, EGaIn, PEDOT:PSS, electric field, noncontact sensing



INTRODUCTION

Noncontact flexible electronics (NFEs) enable touchless human–machine interactions for Internet of Things technology, showing great application potential in many fields, such as real-time monitoring of human physiological signals and noncontact gesture control and recognition.^{1–4} Transforming invisible electric field induction into detectable electrical signal changes has proven to be an effective sensing mechanism for designing NFEs.^{5–7} However, the development of electric field-based NFEs (EF-NFEs) is still in its infancy. Theoretically, the penetration ability of electric fields allows EF-NFEs to detect signal sources far away even when they are physically separated by obstacles, and EF-NFEs can detect any motion that disturbs their electric fields.⁶ Nevertheless, with limited detection distances (usually <20 cm), currently reported EF-

NFEs can only detect finger proximity and nearby hand gestures without any obstacles and often only generate clear electrical signals for a much shorter distance (usually <5 cm).^{3,5,7–10} Obviously, the signal resolution of these EF-NFEs is limited, and to detect everyday human activities, a designed EF-NFE device should possess high spatial resolution to detect movement signals in a large space. Therefore, designing advanced EF-NFEs is becoming an urgent need.

Received: September 1, 2022

Accepted: November 2, 2022

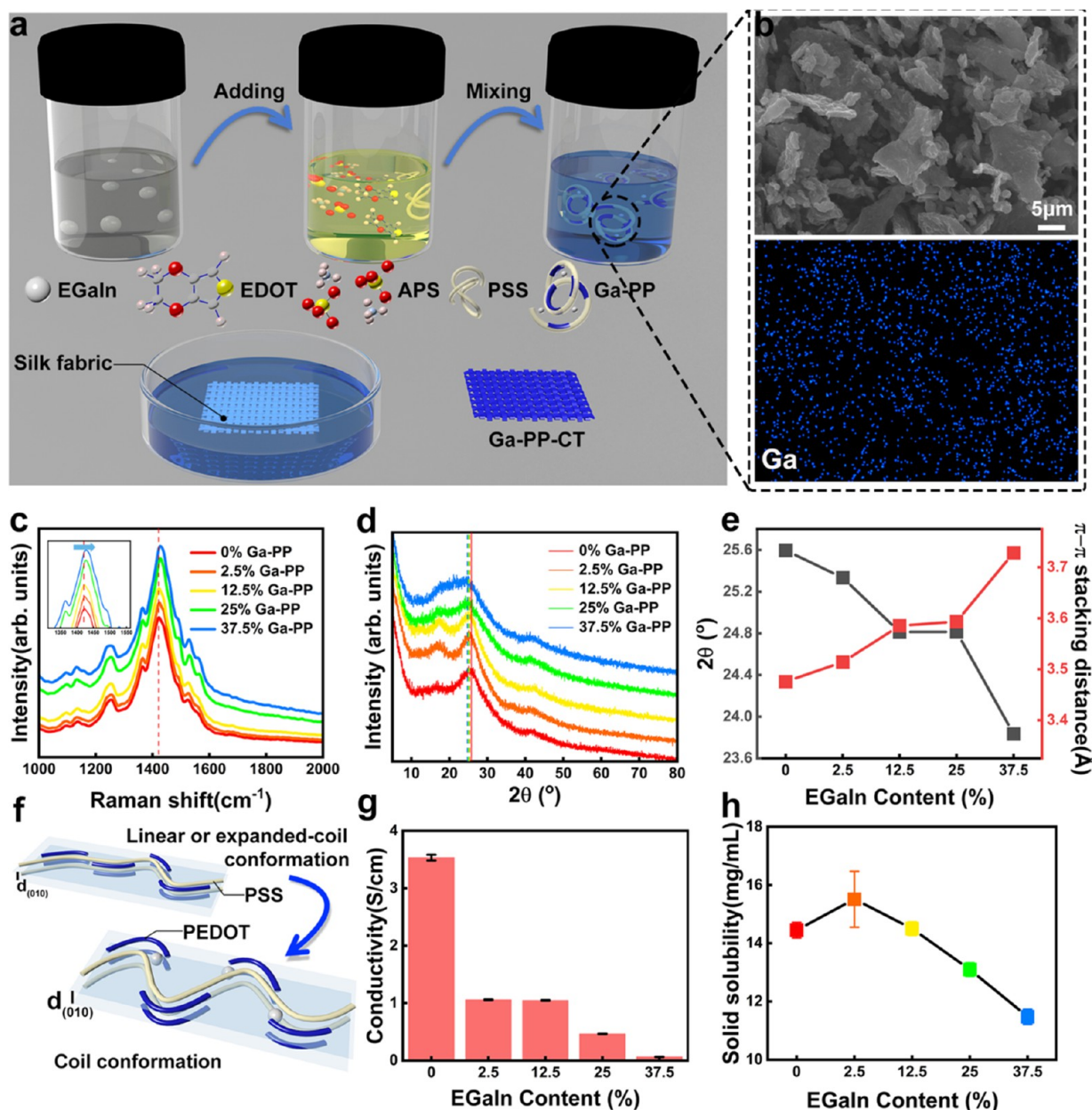


Figure 1. Fabrication and characterization of Ga-PP. (a) Schematic illustration of the Ga-PP and Ga-PP-CT fabrication processes. (b) FESEM and corresponding EDS mapping images of the 12.5% Ga-PP sample. (c) Raman spectra of different Ga-PP samples. (d and e) XRD spectra of different Ga-PP samples (d), and π - π stacking distance of interchain thiophene rings calculated from their XRD spectra (e). (f) Schematic illustration of the conformational change of the PEDOT chains from the linear or expanded-coil conformation to the coil conformation and the increase in the π - π stacking distance of interchain thiophene rings of PEDOT chains after EGaIn is introduced into PEDOT:PSS.^{33,45} Notably, the size of the introduced EGaIn particles is approximately 174 nm (Figure S2b). (g) Conductivity of different Ga-PP samples. (h) Water solubility of different Ga-PP samples.

Essentially, disturbance of the electric field of EF-NFEs can induce charge redistribution, thus generating noncontact sensing signals.^{6,9} Given that the charge redistribution actually stems from electron movement and that the changes in the detected electrical signals, such as the resistance and current, are closely related to the moving electron quantity,³ increasing the induced electron density in EF-NFEs is a straightforward strategy to improve the noncontact sensing performance when EF-NFEs are disturbed by signal sources. Therefore, achieving electron-rich storage in EF-NFEs may lead to more sophisticated control over their electric field induction ability and thus their noncontact sensing ability. A connection

between improved noncontact signals of an EF-NFE sensor and the abundant electron storage in the graphene edges embedded in its sensing layer has been observed in a previous report.⁶ However, actively regulating the electron transport pathways of intra- and intermolecular chains to achieve electron accumulation to prepare EF-NFE materials has rarely been reported.

Poly(3,4-ethylenedioxythiophene):poly(styrenesulfonate) (PEDOT:PSS) is one of the most common conductive polymers used for flexible electronics owing to its good water dispersibility and the versatile applications of its aqueous dispersions.^{11–13} Although segregating PEDOT:PSS chains by

blending them with latex nanospheres to design EF-NFEs has been demonstrated,⁹ the chain segregation strategy based on constructing polymer composites is far from successful in manipulating electron storage. Indeed, tailoring EF-NFE materials with abundant electron storage through molecular chain regulation still remains challenging. Currently, gallium-based liquid metals (Ga LMs) are attractive materials in flexible electronics due to their distinct physicochemical properties,^{14–16} showing potential in changing the intra- and interchain interactions of soft materials to fabricate flexible electronic devices.¹⁷ Hence, adjusting the PEDOT:PSS chain interactions to realize electron accumulation on the chains by utilizing Ga LMs may be an effective strategy for designing EF-NFE materials, thus improving the electric field induction ability and noncontact sensing ability of the obtained EF-NFEs.

Here, we report an interesting material prepared from Ga LMs and PEDOT:PSS (Ga-PP) for fabricating EF-NFEs with improved noncontact sensing performance. Ga-PP shows great potential in designing EF-NFE devices. Without the need to design complex sensor arrays, Ga-PP-based EF-NFE devices can be prepared by immersing commercial silk fabric into Ga-PP solutions for 5 min, indicating that large-scale EF-NFE device production can be achieved with Ga-PP. The obtained devices show a long detection distance (>1 m) and a high spatial resolution, with the ability to trace moving signal sources, and the devices can precisely capture an athlete's movement signals even underwater. A series of experiments are designed to reveal the connection between the electric field induction ability of the devices and their adjusted electron storage achieved through the proposed molecular chain microregulation mechanism. In addition, conductive circuits constructed with Ga-PP ink on planar and curved surfaces also display an accurate noncontact sensing ability, meaning that Ga-PP possesses the potential for EF-NFE fabrication with various patterning and printing technologies. Through a microscopic molecular chain regulation mechanism to achieve electron-rich storage, we successfully improve the electric field sensing ability of EF-NFE materials in this work, providing insights for designing cutting-edge EF-NFEs by regulating the microstructure.

RESULTS AND DISCUSSION

Fabrication and Characterization of Ga-PP. To ensure the introduction of Ga LMs into PEDOT:PSS chains, Ga-PP was fabricated by polymerizing ethylenedioxythiophene (EDOT) monomer solutions containing Ga LMs (Figure 1a and Figure S1) instead of simply mixing Ga LMs with PEDOT:PSS by probe sonication. As a proof of concept, eutectic gallium–indium alloy (EGaIn) was chosen as the Ga LM for Ga-PP fabrication. EGaIn solution was prepared by sonicating an aqueous solution containing bulk EGaIn. Notably, the sonicated EGaIn particles are easily passivated and form an oxidation layer (approximately 1 to 7 nm thick), namely, a Ga₂O₃ layer, in an oxygen-rich environment^{18–20} (Figure S2), thus ensuring the introduction of EGaIn into various soft materials through the interaction between the Ga₂O₃ layer and different polar groups.^{21–23} The obtained EGaIn solution was then added to the EDOT monomer solution containing EDOT, PSS, and ammonium persulfate (APS). The resulting solution was stirred at room temperature for 24 h to fabricate Ga-PP. According to the mass ratio of EGaIn in EDOT, the prepared Ga-PP samples were named

2.5%, 12.5%, 25%, and 37.5%, and the sample without EGaIn, which was pure PEDOT:PSS, was denoted 0%. The successful formation of PEDOT:PSS in Ga-PP samples was confirmed by their Fourier transform infrared (FTIR) spectra, as illustrated in Figure S3. The typical peaks at 1519, 1315, and below 1000 cm⁻¹ are ascribed to C=C asymmetric stretching vibrations, C—C interring stretching vibrations and C—S—C stretching vibrations, respectively, which originate from the thiophene rings of PEDOT. The peaks of C—O—C bending vibrations in the ethylenedioxy groups of PEDOT appear at approximately 1190, 1140, and 1080 cm⁻¹.^{24,25} The incorporation of EGaIn into Ga-PP was verified by X-ray photoelectron spectroscopy (XPS) spectra, with distinct peaks belonging to the Ga element of EGaIn and the oxide layer of Ga₂O₃ being observed, as shown in Figure S4. The incorporation of EGaIn was further revealed by using field emission scanning electron microscopy (FESEM) and energy-dispersive X-ray spectroscopy (EDS) mapping to observe the Ga-PP microstructure. The obtained Ga-PP exhibits a lamellar structure, and the EDS result reveals a uniform distribution of EGaIn in Ga-PP (Figure 1b and Figure S5). The obtained results illustrate that the Ga-PP samples show no significant difference in their microstructure, and EGaIn particles are not observed, while Ga-PP with a higher EGaIn content displays a higher content of uniformly distributed Ga in the corresponding EDS mapping images (Figure S6). Therefore, this synthetic strategy can effectively introduce EGaIn into PEDOT:PSS chains, and Ga-PP is a homogeneous substance rather than a simple mixture.

Insights into the influence of the Ga LM on PEDOT:PSS chains were obtained through X-ray diffraction (XRD) and Raman analysis. PEDOT:PSS consists of conductive conjugated PEDOT chains and insulating PSS chains, so the design strategy for improving the electrical properties of PEDOT:PSS-based electronics mainly targets PEDOT chains.^{11,26} The conformation information on PEDOT chains can be obtained from Raman spectra by analyzing the peak at approximately 1426 cm⁻¹, which corresponds to symmetric C_α=C_β stretching vibrations of the thiophene ring of PEDOT, because a shift in the position of this peak indicates the transformation of the thiophene ring resonant structure between benzoid and quinoid structures²⁷ (Figure S7). These two structures possess different π -conjugation structures and π -electron delocalization degrees, with the benzoid structure favoring a coil conformation and the quinoid structure favoring a linear or expanded-coil conformation.²⁸ As shown in Figure 1c, with increasing EGaIn content in the Ga-PP samples, this peak blue shifts from 1426 to 1434 cm⁻¹, meaning that the added EGaIn tends to induce the transformation of the resonant structure of PEDOT chains from the quinoid to benzoid structure. Therefore, in the presence of EGaIn, the PEDOT chain prefers the coil conformation, implying that the deviation angle between two adjacent thiophene rings on the PEDOT main chain in the plane increases and thus the π - π conjugation degree decreases along the whole PEDOT main chain,²⁹ so the delocalized π -electrons tend to be “stored” in individual thiophene rings. In addition, information on PEDOT interchain interactions influenced by EGaIn was acquired from XRD spectra of Ga-PP samples since the lattice spacing calculated from the distinct peak at a 2θ of approximately 26° corresponds to the π - π stacking distance [$d_{(010)}$] of interchain thiophene rings.^{30–32} The addition of EGaIn causes an increase in $d_{(010)}$, with the $d_{(010)}$ peak shifting to lower angles (Figure

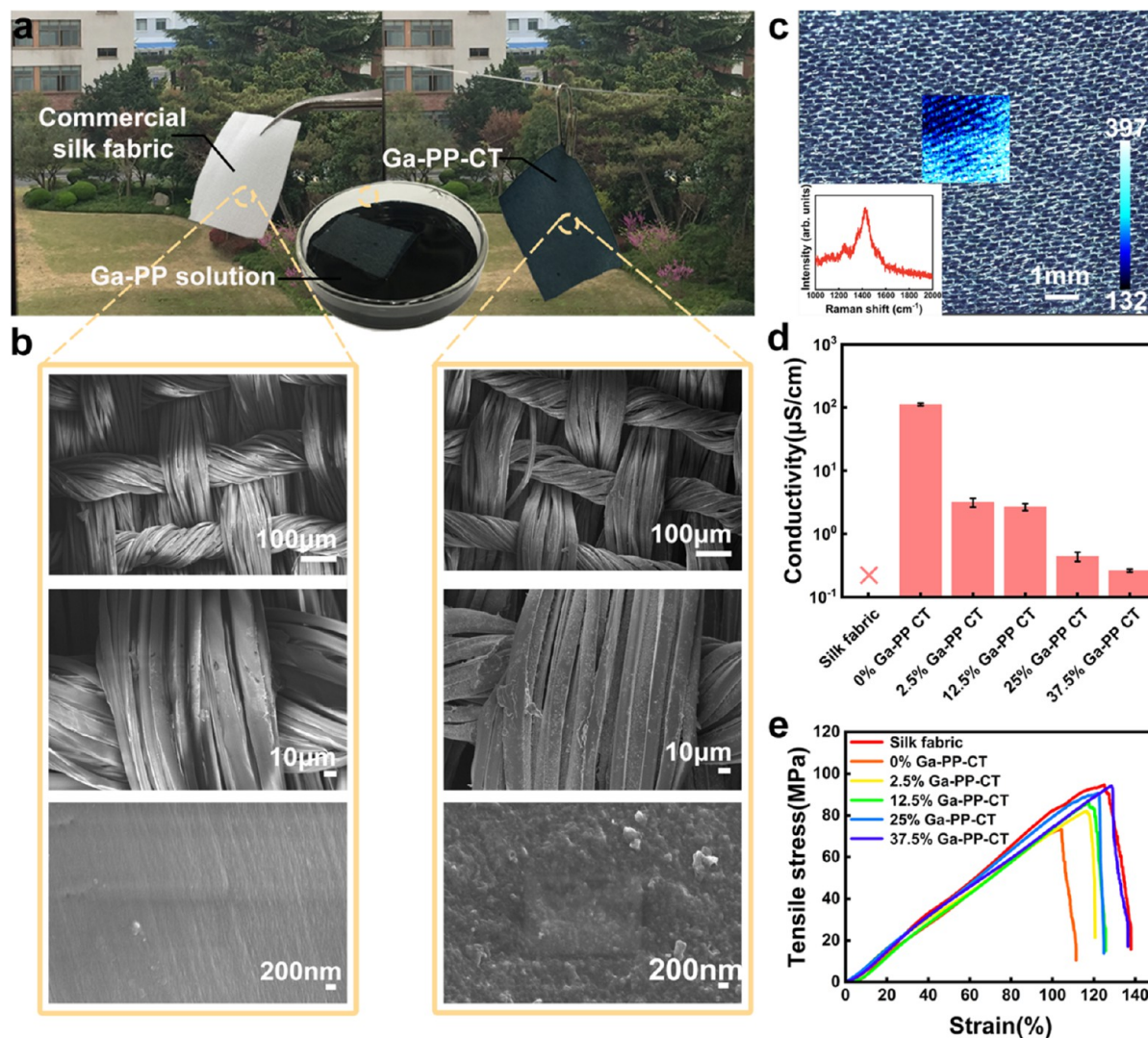


Figure 2. Fabrication and characterization of Ga-PP-CT. (a) Photographs of the Ga-PP-CT fabrication process. (b) FESEM images of 0% Ga-PP-CT and 37.5% Ga-PP-CT with different magnifications. (c) Optical photograph and corresponding Raman mapping results of 12.5% Ga-PP-CT. Inset: Typical Raman spectra of PEDOT. The optical photograph clearly shows the dark blue Ga-PP-CT and its texture. The Raman mapping result is generated by using the Raman intensity of the peak at approximately 1429 cm^{-1} to visualize the Ga-PP distribution on the SF surface. (d) Conductivity of different Ga-PP-CT samples. (e) Stress–strain curves of different Ga-PP-CT samples.

1d,e), suggesting a decrease in the π – π interchain coupling interaction between PEDOT chains and thus a reduction in the π – π interchain charge transfer over an individual thiophene ring.³³ Meanwhile, the conjugated electron information on thiophene rings can also be observed in XPS spectra.³⁴ For 0% Ga-PP, the peaks at 162.58 and 163.67 eV come from the S atoms of the thiophene rings, while these two peaks in 37.5% Ga-PP shift in the high binding energy direction, appearing at 162.87 and 164.17 eV, respectively, indicating a stronger binding interaction between the thiophene rings and their electrons and thus a lower conjugated electron mobility (Figure S8).^{35,36} Notably, the S 2p peaks of PSS also shift toward the high binding energy side in 37.5% Ga-PP, which may result from the transformation of PSS[−] into PSS-EGaIn induced by the electrostatic interaction between sulfonate groups and the Ga₂O₃ layer of EGaIn (Figure S9), similar to the result for protonated PSS (PSSH).^{37,38} Given that PEDOT chains are attached to the PSS chain through the Coulombic interaction,¹¹ the presence of EGaIn during the EDOT polymerization process would

inevitably influence the Coulombic interaction between PSS and the obtained PEDOT to a certain extent. Moreover, the presence of metal oxide particles has been reported to lead to changes in the bending points of PEDOT chains and influence the conjugation length of thiophene rings.³⁹ Therefore, the specific interaction mechanism between PEDOT:PSS and EGaIn can be inferred as follows: (i) due to the combination with PSS being influenced by EGaIn, the bending degree of the prepared PEDOT chains tends to increase, thus adopting a coil conformation to achieve a more stable state during the polymerization process, meaning that the conjugation degree of thiophene rings in PEDOT chains decreases and thus their conjugated π -electrons tend to be stored in thiophene rings; (ii) a reduction in the interchain interaction between PEDOT chains may arise due to the steric hindrance from the added EGaIn during the polymerization process, thus causing an increase in the π – π stacking distance and a decrease in the π – π interchain charge transfer over thiophene rings. Notably, previous studies showed that water can react with EGaIn, thus producing oxidized Ga species (GaOOH) beyond the Ga₂O₃

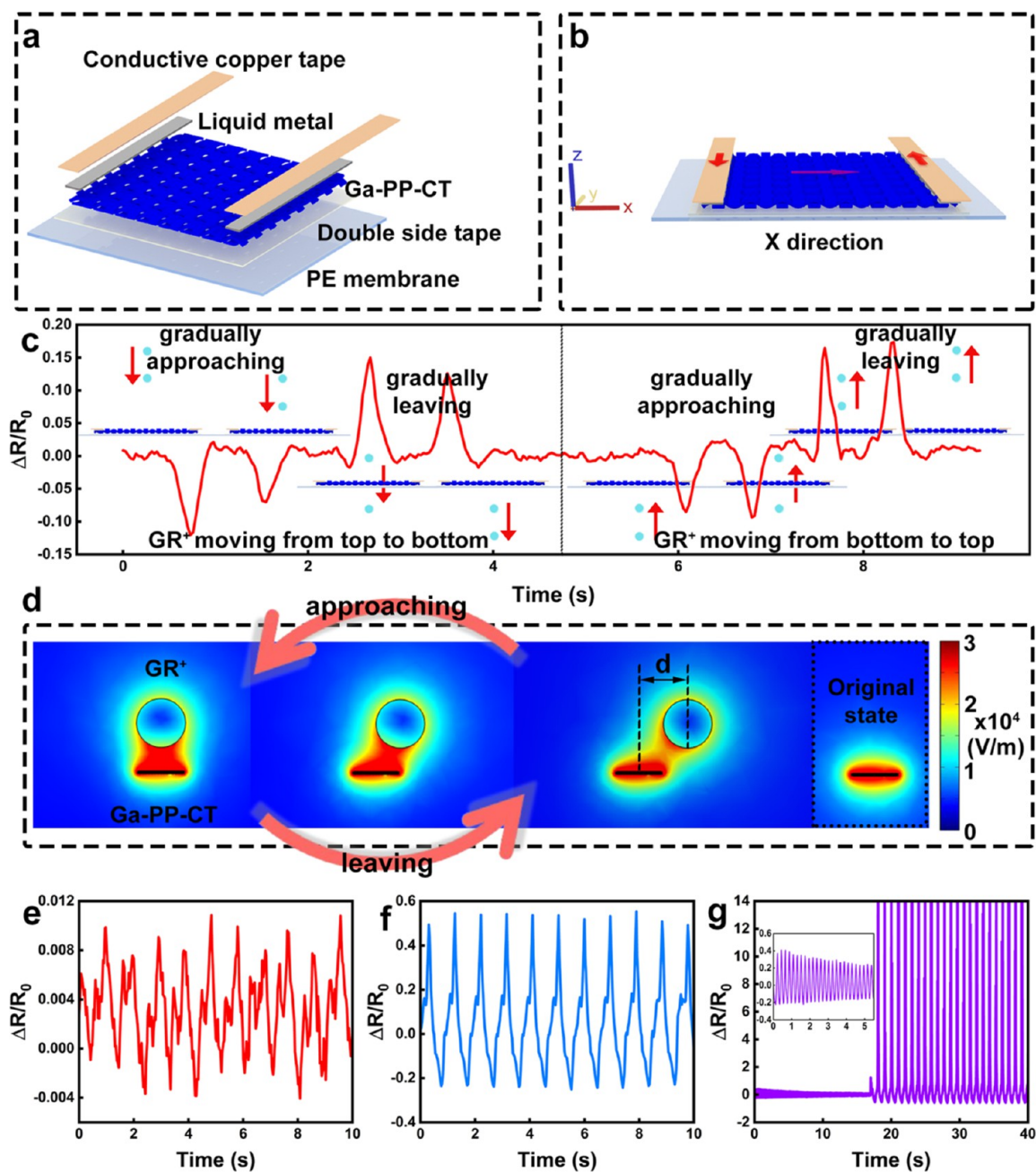


Figure 3. Noncontact sensing rules and mechanism of Ga-PP-CT. (a) Schematic illustration of the preparation of Ga-PP-CT EF-NFEs. (b) Schematic illustration of the spatial coordinates set according to the electrical current direction in Ga-PP-CT. (c) Noncontact sensing response of Ga-PP-CT to translation motion of GR⁺ along the z-direction. Inset: Schematic illustrations of the initial position of GR⁺ and its final position after moving. (d) Simulation results of the change in the electric field of Ga-PP-CT when GR⁺ approaches and moves away along the x-direction. The distance between GR⁺ and Ga-PP-CT in the x-direction is labeled d . Notably, the electric field of Ga-PP-CT is similar to that of negatively charged objects due to the moving electrons on it. (e–g) Noncontact sensing abilities of 0% Ga-PP-CT (e), 12.5% Ga-PP-CT (f), and 37.5% Ga-PP-CT (g) for GR⁺ with a fixed motion state.

oxide,^{40,41} so GaOOH crystallites produced on the EGaln surface may also contribute to the combination of EGaln and PSS by forming hydrogen bond interactions with the sulfonate groups of PSS. Moreover, given that the thiol group is easily assembled on the EGaln surface,^{42–44} thiophene rings on PEDOT may also interact with EGaln due to the increase in the π -electron density of thiophene rings. Therefore, these two interactions may contribute to adjustment of the PEDOT chains, but the detailed interaction mechanism requires further investigation. Thus, in general, the conformational change of

PEDOT chains in Ga-PP can be illustrated as in Figure 1f. Initially, PEDOT:PSS, namely, 0% Ga-PP, possesses both coil and linear or expanded-coil conformations.²⁷ However, the linear or expanded-coil conformation tends to transform into the coil conformation after EGaln is introduced because the presence of EGaln induces resonant structure changes in the thiophene ring on PEDOT chains. With increasing EGaln content, the coil conformation gradually becomes dominant in PEDOT chains. Moreover, the addition of EGaln also causes a decrease in the π – π interchain coupling of PEDOT chains.³³

Therefore, EGaIn can simultaneously regulate the intra- and interchain π -electron transport pathways of PEDOT chains, thus achieving electron accumulation on the chains of the obtained Ga-PP. Clearly, based on the influence of EGaIn on the intra- and interchain interactions of PEDOT discussed above, the π -electrons of the thiophene rings of Ga-PP can be inferred to become more localized at higher EGaIn contents. Hence, the increased “electron storage” is anticipated to endow Ga-PP-based EF-NFEs with higher sensitivity to the stimulus of external electric field variations,⁶ thus generating stronger output signals and showing outstanding noncontact sensing ability.

The conductivity and solubility of Ga-PP were also investigated since the former directly influences the conductivity of the obtained electron devices and the latter can endow Ga-PP with facile solution processability. The addition of EGaIn causes a decrease in the conductivity of Ga-PP as a consequence of the decreased π -electron delocalization degree of PEDOT chains (Figure 1g). However, the minimum conductivity of Ga-PP is still larger than that of the sonicated Ga LM since without the introduction of suitable sintering technologies, the obtained nano/microsized Ga LM particles are insulating due to their separation by encapsulating oxide layers after sonication treatment.¹⁴ The water solubility of Ga-PP also shows a decreasing trend, reaching approximately 11.5 mg/mL for 37.5% Ga-PP (Figure 1h). Notably, the solid content of most commercial PEDOT:PSS solutions is approximately 1.1%–1.5% (11–15 mg/mL). Thus, the water solubility of Ga-PP is comparable to that of commercial PEDOT:PSS, making Ga-PP suitable for various processing techniques in designing flexible electronics.

Preparation and Characterization of Ga-PP EF-NFE devices. Its good water solubility provides Ga-PP with various design possibilities in preparing Ga-PP EF-NFE devices. As a proof of concept, commercial silk fabric (SF) was chosen as a soft substrate to combine with Ga-PP for EF-NFE device fabrication. Ga-PP can be easily combined with SF by soaking SF in a Ga-PP solution for 5 min and then allowing it to dry naturally (Figure 2a). The obtained conductive textiles were named according to the Ga-PP samples used, namely, 0% Ga-PP-CT, 2.5% Ga-PP-CT, *etc.* Attachment of Ga-PP to SF was observed by FESEM (Figure 2b), and a homogeneous distribution of Ga-PP was determined by EDS mapping, as shown in Figure S10. Obviously, Ga-PP does not destroy the whole structure of the SF during the soaking process. Meanwhile, Ga-PP can be tightly deposited on the surface of silk fibers after drying. Compared with the original fiber with a smooth surface, the treated silk fibers clearly show tightly packed Ga-PP on their surfaces. In particular, materials prepared by directly sonicating Ga LMs with polymers usually exhibit phase separation in the dry state due to their different deposition velocities.^{46,47} However, this phenomenon is not observed for the treated fibers, meaning that Ga-PP possesses excellent structural stability and can thus preserve its properties well when processed. In addition, Ga-PP can be inferred to be uniformly distributed over the whole SF from the Raman mapping result (Figure 2c). Intensity differences in the Raman mapping result are inevitable since not all silk fibers are on the focal plane due to the woven structure of SF.⁴⁸ Therefore, the conductivity of Ga-PP-CT stems from the percolated Ga-PP and changes accordingly depending on the attached Ga-PP (Figure 2d).

In addition, the mechanical properties of Ga-PP-CT were investigated. Generally, SF has good mechanical strength, but the mechanical properties of 0% Ga-PP-CT dramatically decrease (Figure 2e). The reason for this is that the ionization of PSS makes the solution acidic, and the acid treatment causes some degree of decomposition of the silk fibers, thus negatively affecting the mechanical properties of SF.⁴⁹ However, an increase in the EGaIn content of Ga-PP contributes to the recovery of the mechanical properties of SF because the mechanical strength of silk fibers can be improved by the interaction with EGaIn through their functional groups, such as carboxyl and hydroxyl groups.^{47,50} The mechanical performance of 37.5% Ga-PP is comparable to that of the original SF, indicating that EGaIn can effectively offset the negative impact of PEDOT:PSS on the mechanical properties of SF (Figure S11). In addition, the conductive and mechanical properties of the hydrogel material can be regulated by Ga-PP, as shown in Figure S12. Therefore, Ga-PP can be inferred to possess the potential to be combined with various soft materials and simultaneously adjust their conductive and mechanical properties for soft electronic device fabrication (Supporting Discussion 1 and Figures S13 and S14).

Noncontact Sensing Sensitivity and Mechanism of Ga-PP-CT. Ga-PP-CT was fixed on a PE membrane to test its noncontact sensing ability under a direct current–voltage (Figure 3a). To systematically study the noncontact sensing sensitivity of Ga-PP-CT to moving objects in three-dimensional space, we set the current direction in Ga-PP-CT as the *x*-direction and determined the *y*-direction and *z*-direction accordingly (Figure 3b). Considering that the electric field direction of positive charges differs from that of negative charges, EF-NFEs should generate different output signals for moving objects with different charges, but few studies currently focus on this aspect. Thus, to systematically explore the noncontact response capability of Ga-PP-CT for signal sources with different charges, a glass rod rubbed with SF was chosen as the research object with a positive charge. When the positively charged glass rod (GR⁺) approached Ga-PP-CT along the *z*-direction, the resistance of Ga-PP-CT decreased, while when GR⁺ moved away along the same path, the resistance of Ga-PP-CT increased (Figure S15 and Video S1). In contrast, the SF acquired a negative charge after rubbing it with the GR, and the resistance change trends of Ga-PP-CT when the negatively charged SF moved along the same trajectory as GR⁺ were completely opposite to those for GR⁺ (Figure S16). Moreover, because the soft SF was difficult to handle and control during the moving process, a polyurethane rubber rod (PUR⁻), which was negatively charged after rubbing it with PE gloves, was used in the following studies. The output signal change trends for SF⁻ movements also apply to PUR⁻ movements. Notably, when the charged objects stop moving, Ga-PP-CT quickly recovers its original resistance value. Based on these experimental results, the noncontact sensing rules of Ga-PP-CT are summarized as follows: (i) positively charged objects approaching Ga-PP-CT and negatively charged objects moving away from Ga-PP-CT cause its resistance to decrease, (ii) positively charged objects moving away from Ga-PP-CT and negatively charged objects approaching Ga-PP-CT cause its resistance to increase, and (iii) static charged objects do not cause resistance changes. To explore the universality and accuracy of the proposed sensing rules, we investigated the noncontact sensing performance of Ga-PP-CT regarding translations of charged objects along

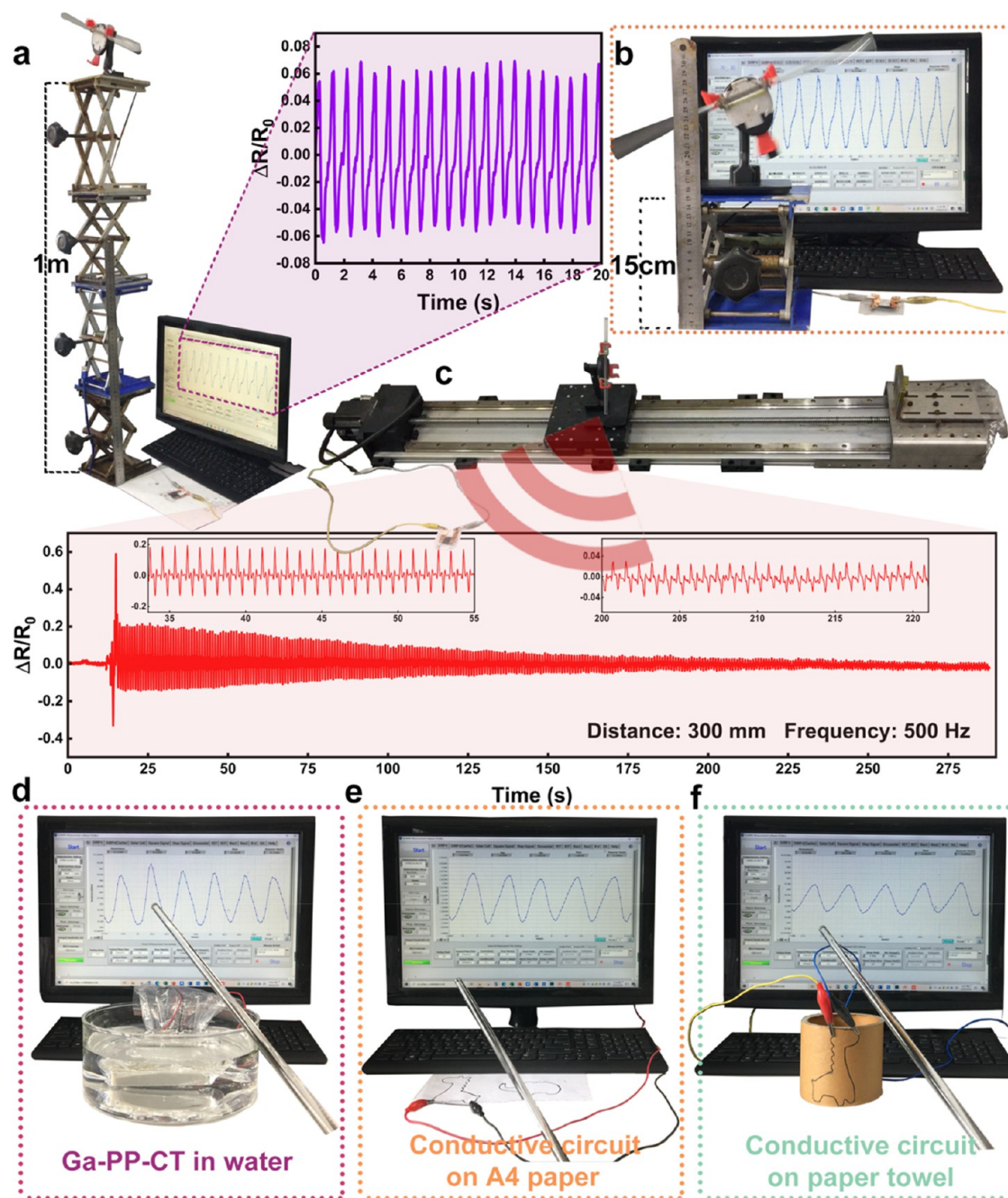


Figure 4. Noncontact sensing ability of Ga-PP-CT. (a) Noncontact sensing signals of Ga-PP-CT when moving GR⁺ 1 m away from it. (b) Noncontact sensing signals of Ga-PP-CT when moving GR⁺ 15 cm away from it. The signal data can be found in [Figure S23](#). (c) Noncontact sensing ability of Ga-PP-CT for moving GR⁺ placed on a moving motorized long-travel translation stage, as shown in the photograph ([Video S7](#)). The moving distance and the moving speed of the translation stage are 300 mm and 500 Hz (approximately 1.25 mm/s), respectively. Inset: Enlarged output signals during different time intervals. (d) Noncontact sensing ability of Ga-PP-CT when placed in water. Notably, Ga-PP-CT was sealed in a closed box before being placed in water to prevent water intake. Clear and repeatable noncontact signals for moving GR⁺ can be observed in the photograph. The signal data can be found in [Figure S26](#). (e and f) Conductive circuits with a noncontact sensing ability drawn with Ga-PP ink on A4 paper (e) and a paper core (f). The signal data can be found in [Figure S27](#).

different directions. Applying a translation motion can ensure that the motion of the charged objects is only in a specific direction and avoid motion-producing components in other directions, so we can carefully investigate the noncontact sensing ability of Ga-PP-CT for charged objects moving in three-dimensional space. Moreover, when the translation distances of the charged objects are sufficiently large in a specific direction, the objects will first approach Ga-PP-CT and then move away from it, and incorporating these two motion

states into a whole moving process can further reveal the noncontact sensing principles of Ga-PP-CT. [Figure 3c](#) and [Figure S17](#) clearly show that the resistance variations of Ga-PP-CT fully accord with the summarized rules when GR⁺ and PUR⁻ are moved from top to bottom or bottom to top along the z-direction ([Video S2](#)). Additionally, experiments in which the charged objects were translated along the x- and y-directions adequately demonstrate the universality and accuracy of the proposed rules ([Figure S18](#), [Videos S3](#) and

S4). Generally, when two objects with different materials contact each other, transfer of charges may occur, so one of the objects becomes positively charged while the other becomes negatively charged.^{51–53} Therefore, the vast majority of objects in daily life have various quantities of different charges, suggesting that Ga-PP-CT can be used to detect the motions of various objects.

The noncontact sensing mechanism of Ga-PP-CT was revealed by using finite element simulation to analyze the electric field variation of Ga-PP-CT when charged objects move. Although the continuous change in the Ga-PP-CT electric field when charged objects move cannot be simulated, the whole variation process of the electric field can be divided into many different transient states to analyze its change rules. In each transient state, the charge quantities of Ga-PP-CT and the charged object are constant, and there is no contact between them nor is any additional charge introduced; thus, the total charge quantities remain unchanged, and on this basis, the simulation was carried out. The simulation results show that in the original state, the electric field of Ga-PP-CT is elliptical and symmetrical from top to bottom, and the electric field strength continuously decreases as the distance above and below Ga-PP-CT increases (Figure 3d). When GR⁺ moves, the electric field of the Ga-PP-CT is induced to change accordingly. When GR⁺ approaches Ga-PP-CT (the distance between GR⁺ and Ga-PP-CT in the *x*-direction, labeled *d*, changes from 2 to 1 and 0 mm), the electric field around Ga-PP-CT is no longer symmetrical and is gradually induced to concentrate on Ga-PP-CT on the GR⁺ side and become stronger. In contrast, GR⁺ moving away tends to make the electric field of Ga-PP-CT “deviate” from Ga-PP-CT, follow GR⁺ and become weaker (*d* changing from 0 to 1 and 2 mm). The change in the electric field illustrates the redistribution of charges on Ga-PP-CT.⁶ A more concentrated and stronger electric field indicates an increased charge density, and the opposite change represents a decreased charge density. According to the definition of current intensity, an increase in the charge quantity on Ga-PP-CT will cause an increase in the current intensity and a decrease in the resistance at a certain moment, whereas a reduction in the charge quantity will lead to the opposite changes in the current and resistance. Obviously, the impacts discussed above on the electric field of Ga-PP-CT and its resistance are reversed when PUR[−] moves (Figure S19). Therefore, the proposed noncontact sensing rules of Ga-PP-CT previously mentioned can be well explained by the obtained simulation results. Notably, Ga-PP-CT cannot detect stationary charged objects since the electrostatic field of charged objects cannot induce charge rearrangement in Ga-PP-CT. In contrast, moving charged objects generate a change in the electric field, thus producing a magnetic field accordingly, so the produced electromagnetic field interacts with that of Ga-PP-CT to induce charge density redistribution on Ga-PP-CT.

Moreover, the charge redistribution on Ga-PP-CT actually originates from movement of its electrons. Thus, the noncontact sensing abilities of different Ga-PP-CT samples for charged objects with the same motion were measured to explore the relationship between the electron storage and the noncontact sensing performance. The rotation motion of GR⁺ was fixed by a customized device, as shown in Figure S20. Using this device, the straight-line distance between the lowest and highest points in the GR⁺ rotation process can reach approximately 15 cm. Figure 3e–g and Figure S21 show that, when GR⁺ rotates with the maximum amplitude, Ga-PP-CT

samples with higher EGaIn contents show increased sensing sensitivity and signal strength. The generated signal strengths of 25% and 37.5% Ga-PP-CT are approximately 1000 times larger than that of 0% Ga-PP-CT. Even when GR⁺ moves with a much smaller amplitude (approximately 3 cm), 25% and 37.5% Ga-PP-CT can still produce clear and repeatable signals, as shown in the inset of Figure 3g and Figure S21b (Video S5). The noncontact sensing ability of Ga-PP-CT mainly depends on Ga-PP attached to silk fibers. Thus, as discussed above, Ga-PP-CT with a higher EGaIn content tends to possess higher electron storage due to the increased π -electron accumulation on the PEDOT chains of Ga-PP induced by EGaIn. When suffering the same disturbance induced by signal sources, Ga-PP-CT with higher electron storage can generate stronger output signals due to the increase in the induced electron density. Meanwhile, the improved electron storage also benefits capture of tiny disturbances by Ga-PP-CT, thus contributing to a larger detection distance. Therefore, the increase in the accumulated electrons resulting from the decreased delocalization degree can be inferred to provide a higher sensitive to external electric field changes, and an increase in the induced electron density can be inferred to contribute to producing clearer signals. The influence of electron storage on the noncontact sensing ability can also be found in graphene-based noncontact sensors.⁶ Hence, achieving microregulation of PEDOT chains by EGaIn can be inferred to be an effective strategy for preparing EF-NFEs with higher noncontact sensing ability. Predictably, moving charged objects with different charge quantities show different influences on the electric field of Ga-PP-CT (Figure S22).

Noncontact Sensing Applications of Ga-PP-CT. The noncontact detection distance is a significant parameter for noncontact sensors, which directly influences their practical application. Compared with previously reported EF-NFEs, the detection distance of Ga-PP-CT is greater than 1 m (Figure 4a and Table S1). As the distance between the moving charged object and Ga-PP-CT increases, the generated output signal strength of Ga-PP-CT shows a decreasing trend (Figure 4b and Figure S23). When the detection distance increases from 0 to 20 cm, the detection signal strength dramatically decreases, while as the distance continues to increase to approximately 1 m, the signal strength slowly decreases (Figure S24). However, the remaining signal strength at 1 m is still clear enough to be distinguished. Only when the distance exceeds 1 m will the output signal become too weak to detect (Video S6). Hence, achieving an increase in the electron storage of EF-NFEs is clearly an attractive strategy to improve their sensitivity to electric field changes, thus endowing them with the ability to capture tiny disturbances in their electric field. Therefore, Ga-PP-CT shows amazing noncontact sensing performance in detecting a signal source 1 m away. Moreover, Ga-PP-CT can not only detect different motion states of moving objects but also trace the continuous position changes of moving charged objects in three-dimensional space (Figure 4c, Figure S25, and Video S7). As the moving distance of the translation stage that the moving GR⁺ is placed on increases, the moving GR⁺ continues to move away from Ga-PP-CT, and the whole process can be reflected in the decreasing output signal strength of Ga-PP-CT. Therefore, Ga-PP-CT possesses the potential to detect complex motions of charged objects in three-dimensional space. Considering that the electric field of Ga-PP-CT is not a uniform spherical field, Ga-PP-CT should produce different noncontact signal data when moving charged

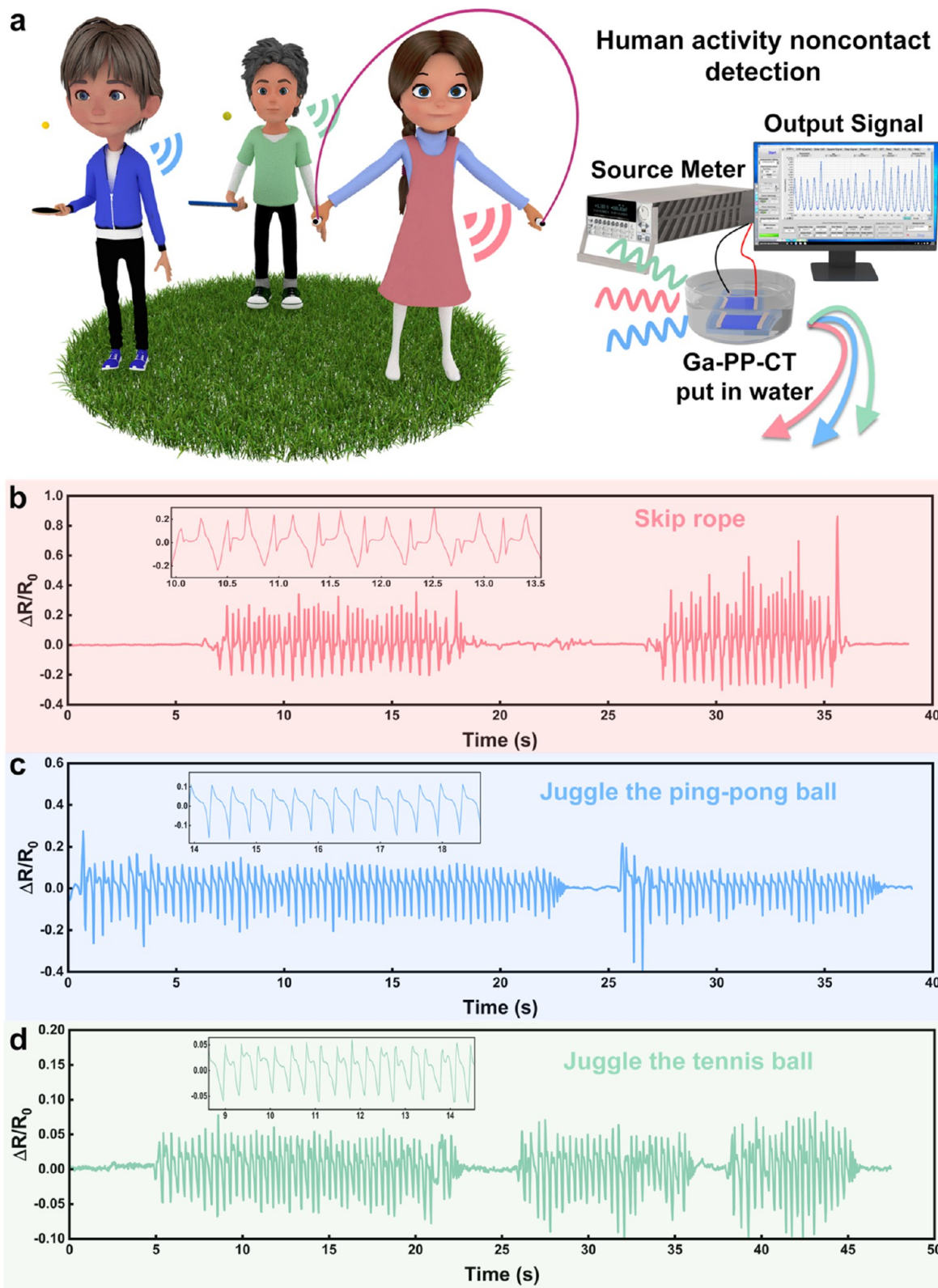


Figure 5. Noncontact sensing applications of Ga-PP-CT. (a) Schematic illustration of noncontact sensing applications of Ga-PP-CT to identify different sports (Video S10). (b–d) Noncontact sensing signals generated by Ga-PP-CT when the volunteer skips rope (b), juggles a ping-pong ball (c), and juggles a tennis ball (d). Insets: Enlarged noncontact signals.

objects are located at different positions, meaning that, by designing suitable signal decoupling technologies, the precise locations of moving charged objects can be calculated by analyzing the output sensing data. In addition, the acute

noncontact sensing ability and the greater penetration ability of electric fields allow Ga-PP-CT to sense moving charged objects even when Ga-PP-CT is placed in water or sealed in a box, meaning that Ga-PP-CT possesses the potential to work in

different complex environments to perform noncontact remote sensing (Figure 4d, Figure S26, and Video S8).

Moreover, due to the excellent water solubility of Ga-PP, its water solution can be used as ink in a rollerball pen to draw conductive circuits. Amazingly, circuits drawn on paper or a paper core also display a noncontact sensing ability (Figure 4e,f, Figure S27, and Video S9), so a conductive circuit with a noncontact sensing ability can be conveniently constructed on a planar or curved surface by using Ga-PP ink. To further illustrate the practical application of Ga-PP ink, a commercial conductive ink, Bare Conductive Electric Paint, which has proven useful in preparing nonconductive sensors, was purchased to construct conductive circuits to compare their noncontact sensing performances. The giraffe-shaped conductive circuits drawn with Electric Paint cannot generate distinguishable electrical signals due to the insufficient Electric Paint. Only when a considerable amount of Electric Paint is used to construct the conductive circuits can the obtained circuits produce a clear electrical signal (Figure S28). In contrast, Ga-PP-based conductive circuits with a few simple lines can generate clearer and stronger detection signals. Therefore, Ga-PP can be inferred to be more suitable for constructing noncontact sensing conductive circuits anywhere that ink can be applied, showing potential to be incorporated into an electrical network of smart devices to support noncontact human–machine interactions.

Considering that the electrostatically charged human body can be seen as a natural signal source and that the movement of the human body will lead to a redistributed electric field nearby, EF-NFEs show great potential in noncontact detection of human activities. However, human activities often involve a large space. With limited detection distances, current EF-NFEs can only capture those activities occurring within their detection range, so previously reported EF-NFEs can only be used to detect finger proximity or hand gestures in a narrow distance range. Given that daily human activities are complex, when the human motion distance increases, these EF-NFEs fail to generate detection signals. Obviously, their spatial resolution is limited, far from being used in detecting everyday human activities. To demonstrate the applications of Ga-PP, Ga-PP-CT was used to detect different physical exercises. Ga-PP-CT can track the process of volunteers playing different sports (Figure 5a and Video S10). When a volunteer begins skipping rope, Ga-PP-CT generates corresponding sensing signals, and when the volunteer stops, Ga-PP-CT quickly recovers its resistance state (Figure 5b). The obtained signal strength and frequency are closely related to the volunteer's performance in the process of skipping rope. In addition, the process of juggling ping-pong balls or tennis balls can be recorded by Ga-PP-CT (Figure 5c,d). Notably, Ga-PP-CT produces different signal shapes for different sports, so its noncontact sensing signals also contain information on the motion types of the charged objects, meaning that Ga-PP-CT can not only detect the precise positions of charged objects but also distinguish their motion types. Therefore, compared with previously reported EF-NFEs, we successfully demonstrate that Ga-PP-CT can be used to monitor the movement signals of athletes in different sporting events. Notably, Ga-PP-CT was placed in water in the above sensing experiments, so it may also be suitable for monitoring underwater sporting events. Hence, we successfully show the potential application of Ga-PP-CT to detect different human activities.

CONCLUSION

In summary, we report a conductive polymer chain micro-regulation mechanism to design conductive materials with improved electron storage for EF-NFEs with high spatial resolution. The intra- and interchain interactions of PEDOT chains are successfully adjusted by introducing EGaIn to achieve electron accumulation on the chains, based on which an attractive conductive material, Ga-PP, is prepared. Without designing complex sensor arrays, the Ga-PP-based noncontact sensor can be easily fabricated by soaking fabric in a Ga-PP solution. The obtained Ga-PP-CT with a noncontact detection distance exceeding 1 m can not only accurately trace continuous changes in the positions and motion states of charged objects but also work properly even when embedded in water. The investigations of the noncontact sensing performance of Ga-PP-CT successfully reveal the relationship between the high noncontact sensing sensitivity and the increased electron storage. Meanwhile, its abundant electron storage endows Ga-PP with the ability to construct conductive circuits with a noncontact sensing ability. We further demonstrate the potential of Ga-PP in identifying different physical exercises. Therefore, Ga-PP possesses vast design possibilities in EF-NFEs, ranging from incorporation into the electrical networks of intelligent devices to noncontact remote sensing, thus offering interesting human–machine interaction possibilities.

EXPERIMENTAL PROCEDURES

Materials. EDOT and EGaIn were purchased from Bide Pharmatech Ltd. and Shenyang Jiabei Commerce Ltd., respectively. PSS (M.W. 75000) and APS were obtained from Alfa Aesar and Sinopharm Chemical Reagent Co., Ltd., respectively. SF was purchased from the Sichouzhilu 7187 store on the Taobao E-commerce Trading Platform.

Fabrication of Ga-PP. First, 0.68 g of PSS was dissolved in 6 g of deionized water, and then, 0.4 g of EDOT was added dropwise into the obtained PSS solution under continuous stirring. Then, 1 g of APS was added and dissolved, followed by the addition of 4 mL of an EGaIn solution. The reaction solution was stirred for 24 h at room temperature to polymerize EDOT. Finally, Ga-PP powder was obtained by vacuum suction filtration to remove redundant reagents and lyophilization. EGaIn solutions were prepared by adding a specific mass of EGaIn to 4 g of deionized water and then applying probe sonication to break up the bulk EGaIn (15 min, 20% power output, ultrasonic cell disruptor JYD-1800L with a 6 mm ϕ probe, Shanghai Zhixin Instrument Co., Ltd.). The 0% Ga-PP, 2.5% Ga-PP, 12.5% Ga-PP, 25% Ga-PP, and 37.5% Ga-PP samples required 0, 0.01, 0.05, 0.1, and 0.15 g of EGaIn, respectively. Notably, EGaIn solutions should be used as early as possible after sonication to prevent precipitation of EGaIn.

Fabrication of Ga-PP-CT. First, a Ga-PP solution with a mass fraction of 1% was prepared, and then, the cut SF was soaked in the prepared Ga-PP solution for 5 min, followed by natural drying. Notably, with increasing soaking time, the mechanical properties of silk fibers may decrease, so the optimal soaking time is 5 min. Additionally, regulation of the conductive and mechanical properties of Ga-PP-CT can be achieved by using different Ga-PP solutions, so we only soaked the SF in the Ga-PP solution for 5 min.

Fabrication of Ga-PP-CT NFEs for Noncontact Sensing Tests. Ga-PP-CT was fixed on a piece of PE membrane that was cut from a PE transparent plastic ziplock valve bag with double-sided tape to protect Ga-PP-CT from contamination. Subsequently, EGaIn was applied to Ga-PP-CT before placing conductive copper tape on the sample to reduce the contact resistance between Ga-PP-CT and the copper tape.

Fabrication of Ga-PP Conductive Circuits. Ga-PP possesses good water solubility, so a 1% Ga-PP solution can act as conductive ink, which can be injected into the empty tube of a roller ball pen to draw a conductive circuit.

Characterization. Images of the morphologies of Ga-PP and Ga-PP-CT and the distribution of Ga in them were collected by FESEM (Zeiss Gemini SEM500) equipped with EDS (EDS Aztec X-Max Extreme EDS), and the data were collected and analyzed by ZEISS SmartSEM User Interface v.6.01 and RemCon 32 software. High-resolution transmission electron microscopy (HRTEM) images of the sonicated EGaIn particles and the corresponding element mapping results were obtained with an FEI Tecnai F20. The FTIR spectra of Ga-PP were recorded using a Thermo Scientific Nicolet iS10 and treated by Omnic v.8.2 software. The Raman spectra of Ga-PP were recorded by a Renishaw In Via Qontor confocal Raman microscope that used a 785 nm excitation laser (1 s exposure time, 0.1% laser power for a single Raman spectrum; 0.1 s exposure time, 1% laser power for Raman mapping spectra), and the obtained Raman results were analyzed by WIRE 5.3 software. XRD spectra of Ga-PP were obtained using a Bruker D8 ADVANCE X-ray diffractometer with Cu K α radiation, and the π - π stacking distance of Ga-PP was calculated by Jade 6.1 software. XPS spectra of Ga-PP were recorded with a Thermo Scientific K-Alpha with Al K α radiation, and the collected XPS results were analyzed with XPSPEAK 4.1 software. The conductivities of Ga-PP and Ga-PP-CT were measured by four-probe resistivity test systems (ST2241 and ST2463). To measure the conductivity of Ga-PP, Ga-PP powder was first pressed into a tablet (radius, 13 mm; thickness, approximately 0.5 mm), and the thickness of Ga-PP-CT was approximately 0.2 mm. To measure the water solubility of Ga-PP, 1 mL of a Ga-PP saturated solution was dried in an oven at 70 °C until a steady mass was obtained. The mechanical properties of Ga-PP-CT were tested using an Instron 5966 tensile tester equipped with a 1 kN load cell at a loading rate of 10 mm/min, in which Ga-PP-CT was cut into strips with dimensions of approximately 15 mm \times 5 mm for the test, and the obtained data were analyzed by Instron Bluehill Universal v.4.08 software.

Simulations Based on the Finite Element Method (FEM).

The electric field variation of Ga-PP-CT during the moving process of charged objects was simulated *via* the Electrostatics module of COMSOL Multiphysics software. The physical field was set up as shown in Figure S29. The length, width, and height of the physical field were 30 mm (*x*-direction), 10 mm (*y*-direction), and 14 mm (*z*-direction), respectively. A boundary area of the physical field with a 1 mm thickness was set up as an infinite element domain. All boundaries of this model were set as grounds. The diameter and height of the dielectric rod were 2 mm (*x*-direction) and 3 mm (*y*-direction), respectively. A simplified three-dimensional model of Ga-PP-CT was created according to its SEM images. The distances in the *y*-direction and *z*-direction between Ga-PP-CT and the dielectric rod were fixed at 0 and 1 mm, respectively. The distance in the *x*-direction between Ga-PP-CT and the dielectric rod was labeled *d*, where *d* = 0, 1, and 2 mm. The relative permittivities of Ga-PP-CT and the dielectric rod were $\epsilon_{r-Ga-PP-CT} = 91.58$ and $\epsilon_{r-rod} = 2.10$, respectively. The space charge densities of Ga-PP-CT and the dielectric rod were $\rho_{V-fabric} = +0.01$ C/m³ and $\rho_{V-rod} = \pm 0.0005$ C/m³ (− for the GR⁺ study, + for the PUR[−] study), respectively. The electric field variation of Ga-PP-CT during the moving process of the charged objects was described using the following equations:

$$\begin{aligned}\nabla \cdot D &= \rho_V \\ E &= -\nabla V \\ D &= \epsilon_0 \epsilon_r E\end{aligned}$$

where ∇ is the Laplace operator, *D* is the electric displacement, ρ_V is the space charge density, *E* is the electric field, *V* is the electric potential, and ϵ_0 and ϵ_r are the permittivities of vacuum and the materials (Ga-PP-CT and the dielectric rod).

Noncontact Sensing Tests. For the noncontact sensing tests, the real-time resistance-time curves of Ga-PP-CT and Ga-PP-based conductive circuits were acquired using a Keithley 2604B

SourceMeter instrument controlled by Ke2600S measurement software v.6.21 (Wuhan Zeal Young Technology Co., Ltd.). In noncontact sensing experiments, the applied voltage was set to 0.4 V in the software interface. Unless otherwise stated, noncontact sensing experiments were carried out using 2.5% Ga-PP-CT. GR⁺ was prepared by rubbing a GR with SF, and PUR[−] was prepared by rubbing a PUR with disposable PE gloves. The rubbing time was fixed at 30 s unless otherwise stated. The customized moving device shown in Figure S20 was used in the following noncontact sensing experiments: (i) exploring the noncontact sensing abilities of different Ga-PP-CT samples, (ii) exploring the influence of the charge quantity of moving objects on the noncontact signal strength of Ga-PP-CT, (iii) exploring the detection distance of Ga-PP-CT, and (iv) exploring the noncontact sensing ability of Ga-PP-CT for a moving signal source. In other noncontact sensing experiments, the movements of GR⁺ and PUR[−] were controlled by hand to demonstrate the noncontact sensing performance of Ga-PP-CT and Ga-PP-based conductive circuits. In experiments exploring the noncontact sensing ability of Ga-PP-CT for GR⁺ with different charge quantities, the amount of positive charge on the GR was regulated by controlling the rubbing time between the GR and SF. In addition, the GR that had been washed with water to remove the charge on it was used as the control. The strength of the produced electric field when GR/GR⁺ moved was measured by an electromagnetic field tester (LZT-1000, Beijing Longzhentian Electronic Instrument Co., Ltd.). Notably, since the rubbing strength and speed controlled by hand cannot be fully consistent, the charge transfer amount between the GR and SF may differ at the same rubbing time, thus leading to a difference in the produced electric field strength when GR⁺ moves in each test. However, the increasing trend of the obtained electric field strength with increasing rubbing time was stable (Figure S22d), so the investigation that explored the noncontact sensing ability of Ga-PP-CT for moving objects with different charge quantities could not be influenced.

ASSOCIATED CONTENT

Supporting Information

The Supporting Information is available free of charge at <https://pubs.acs.org/doi/10.1021/acsnano.2c08760>.

Figures of color evolution of the reaction solution, FESEM and HRTEM images, size distributions, elemental mapping results, FTIR spectra, XPS spectra, EDS mapping images, content of Ga element calculated from the EDS results of different Ga-PP samples, benzoid and quinoid resonant structures, schematic illustration of the interaction between EGaIn and PEDOT:PSS, tensile strength and maximum tensile strain of different Ga-PP-CT samples, characterization of Ga-PP-based hydrogels, strain sensitivity of Ga-PP-CT, noncontact sensing responses of Ga-PP-CT to the moving GR⁺ and the moving negatively charged SF and PUR[−], simulation results of the electric field change of Ga-PP-CT, photograph of the GR⁺ rotation device and the schematic illustration the rotation process of GR⁺, noncontact sensing abilities of 2.5% Ga-PP-CT and 25% Ga-PP-CT, noncontact sensing signals of Ga-PP-CT, maximum output signal value at different detection distance, noncontact sensing signals of Ga-PP-CT, and overall calculation model created for FEM simulations, discussions of strain sensing ability and applications of Ga-PP-CT and experimental details, and table of comparison of the maximum detection distance of different NFEs in current literatures (PDF)

Video of noncontact sensing response of Ga-PP-CT to the moving GR⁺ (MP4)

Video of noncontact sensing response of Ga-PP-CT toward the translation motions of GR⁺ along the z-direction (MP4)

Video of noncontact sensing response of Ga-PP-CT toward the translation motions of GR⁺ along the x-direction (MP4)

Video of noncontact sensing response of Ga-PP-CT toward the translation motions of GR⁺ along the y-direction (MP4)

Video of noncontact sensing abilities of 12.5% Ga-PP-CT towards GR⁺ with a fixed motion state (MP4)

Video of Ga-PP-CT noncontact sensing detecting distance experiments (MP4)

Video of noncontact sensing ability of Ga-PP-CT to the moving GR⁺ that was put on a moving motorized long-travel translation stage (MP4)

Video of noncontact sensing ability of Ga-PP-CT when being put in water (MP4)

Video of conductive circuits with noncontact sensing ability painted by Ga-PP ink printed on the A4 paper (MP4)

Video of noncontact sensing applications of Ga-PP-CT to detect different sports (MP4)

AUTHOR INFORMATION

Corresponding Authors

Jianfeng Shen – Institute of Special Materials and Technology, Fudan University, Shanghai 200433, P. R. China; orcid.org/0000-0002-8835-6292; Email: jfshen@fudan.edu.cn

Mingxin Ye – Institute of Special Materials and Technology, Fudan University, Shanghai 200433, P. R. China; orcid.org/0000-0002-4532-2594; Email: mxye@fudan.edu.cn

Authors

Bin Chen – Institute of Special Materials and Technology, Fudan University, Shanghai 200433, P. R. China; Department of Chemistry, Fudan University, Shanghai 200433, P. R. China

Minying Wu – Department of Chemistry, Fudan University, Shanghai 200433, P. R. China

Shenwen Fang – College of Chemistry and Chemical Engineering, Southwest Petroleum University, Chengdu 610500, P. R. China

Yudong Cao – Institute of Special Materials and Technology, Fudan University, Shanghai 200433, P. R. China; Department of Chemistry, Fudan University, Shanghai 200433, P. R. China

Liyuan Pei – Institute of Special Materials and Technology, Fudan University, Shanghai 200433, P. R. China

Haibin Zhong – Institute of Special Materials and Technology, Fudan University, Shanghai 200433, P. R. China

Chang Sun – State Key Laboratory of Molecular Engineering of Polymers, Department of Macromolecular Science, Fudan University, Shanghai 200433, P. R. China

Xianglong Lin – Institute of Special Materials and Technology, Fudan University, Shanghai 200433, P. R. China

Xuanyang Li – Institute of Special Materials and Technology, Fudan University, Shanghai 200433, P. R. China; Department of Chemistry, Fudan University, Shanghai 200433, P. R. China

Complete contact information is available at: <https://pubs.acs.org/10.1021/acsnano.2c08760>

Author Contributions

B.C. conceived and designed the work, prepared Ga-PP and Ga-PP-CT, conducted sensing experiments and contributed to manuscript writing. M.W. and S.F. were responsible for SEM measurements and contributed to the discussion of Ga-PP synthesis mechanism. Y.C. and H.Z. were responsible for preparing the supporting videos. L.P. was responsible for the experiments of Ga-PP PAM hydrogels. C.S. and X.L. performed Raman, FTIR, and XRD tests and analyzed related data. M.Y. and J.S. contributed to the explanation of noncontact sensing mechanism and funded this work.

Notes

The authors declare no competing financial interest.

ACKNOWLEDGMENTS

The authors deeply thank Professor Hongdong Zhang, Professor Yongmin He, and Professor Caitian Gao for evaluating our work and modifying the manuscript. The authors would also like to thank Professor Kaiyuan Wang from Shiyanjia Lab (www.shiyanjia.com) for performing FEM simulations and discussing relevant sensing mechanism with us. The authors greatly appreciate the financial and spiritual support from Rifeng Chen and Huaqing Feng. This work was also financially supported by National Natural Science Foundation of China (51972064).

REFERENCES

- (1) Lu, L.; Jiang, C.; Hu, G.; Liu, J.; Yang, B. Flexible Noncontact Sensing for Human-Machine Interaction. *Adv. Mater.* **2021**, *33*, 2100218.
- (2) Liu, R.; Lai, Y.; Li, S.; Wu, F.; Shao, J.; Liu, D.; Dong, X.; Wang, J.; Wang, Z. L. Ultrathin, Transparent, and Robust Self-healing Electronic Skins for Tactile and Non-contact Sensing. *Nano Energy* **2022**, *95*, 107056.
- (3) Tang, Y.; Zhou, H.; Sun, X.; Diao, N.; Wang, J.; Zhang, B.; Qin, C.; Liang, E.; Mao, Y. Triboelectric Touch-Free Screen Sensor for Noncontact Gesture Recognizing. *Adv. Funct. Mater.* **2020**, *30*, 1907893.
- (4) Zheng, Y.-N.; Yu, Z.; Mao, G.; Li, Y.; Pravarthana, D.; Asghar, W.; Liu, Y.; Qu, S.; Shang, J.; Li, R.-W. A Wearable Capacitive Sensor Based on Ring/Disk-Shaped Electrode and Porous Dielectric for Noncontact Healthcare Monitoring. *Global Challenges* **2020**, *4*, 1900079.
- (5) Sarwar, M. S.; Dobashi, Y.; Preston, C.; Wyss, J. K. M.; Mirabbasi, S.; Madden, J. D. W. Bend, Stretch, and Touch: Locating a Finger on an Actively Deformed Transparent Sensor Array. *Sci. Adv.* **2017**, *3*, No. e1602200.
- (6) Chen, S.; Wang, Y.; Yang, L.; Guo, Y.; Wang, M.; Sun, K. Flexible and Transparent Sensors with Hierarchically Micro-nano Texture for Touchless Sensing and Controlling. *Nano Energy* **2021**, *82*, 105719.
- (7) Guan, F.; Xie, Y.; Wu, H.; Meng, Y.; Shi, Y.; Gao, M.; Zhang, Z.; Chen, S.; Chen, Y.; Wang, H.; Pei, Q. Silver Nanowire-Bacterial Cellulose Composite Fiber-Based Sensor for Highly Sensitive Detection of Pressure and Proximity. *ACS Nano* **2020**, *14*, 15428–15439.
- (8) Guo, H.; Tan, Y. J.; Chen, G.; Wang, Z.; Susanto, G. J.; See, H. H.; Yang, Z.; Lim, Z. W.; Yang, L.; Tee, B. C. K. Artificially Innervated Self-healing Foams As Synthetic Piezo-impedance Sensor Skins. *Nat. Commun.* **2020**, *11*, 5747.
- (9) Wang, Z.; Wang, T.; Zhuang, M.; Xu, H. Stretchable Polymer Composite with a 3D Segregated Structure of PEDOT:PSS for

Multifunctional Touchless Sensing. *ACS Appl. Mater. Interfaces* **2019**, *11*, 45301–45309.

(10) Zhao, P.; Zhang, R.; Tong, Y.; Zhao, X.; Zhang, T.; Tang, Q.; Liu, Y. Strain-Discriminable Pressure/Proximity Sensing of Transparent Stretchable Electronic Skin Based on PEDOT:PSS/SWCNT Electrodes. *ACS Appl. Mater. Interfaces* **2020**, *12*, 55083–55093.

(11) Fan, Z.; Ouyang, J. Thermoelectric Properties of PEDOT:PSS. *Adv. Electron. Mater.* **2019**, *5*, 1800769.

(12) Wang, Y.; Zhu, C.; Pfattner, R.; Yan, H.; Jin, L.; Chen, S.; Molina-Lopez, F.; Lissel, F.; Liu, J.; Rabiah, N. I.; Chen, Z.; Chung, J. W.; Linder, C.; Toney, M. F.; Murmann, B.; Bao, Z. A Highly Stretchable, Transparent, and Conductive Polymer. *Sci. Adv.* **2017**, *3*, No. e1602076.

(13) Lu, B.; Yuk, H.; Lin, S.; Jian, N.; Qu, K.; Xu, J.; Zhao, X. Pure PEDOT:PSS Hydrogels. *Nat. Commun.* **2019**, *10*, 1043.

(14) Park, Y.-G.; Lee, G.-Y.; Jang, J.; Yun, S. M.; Kim, E.; Park, J.-U. Liquid Metal-Based Soft Electronics for Wearable Healthcare. *Adv. Healthcare Mater.* **2021**, *10*, 2002280.

(15) Wang, C.; Wang, C.; Huang, Z.; Xu, S. Materials and Structures toward Soft Electronics. *Adv. Mater.* **2018**, *30*, 1801368.

(16) Song, H.; Kim, T.; Kang, S.; Jin, H.; Lee, K.; Yoon, H. J. Ga-Based Liquid Metal Micro/Nanoparticles: Recent Advances and Applications. *Small* **2020**, *16*, 1903391.

(17) Chen, B.; Cao, Y.; Li, Q.; Yan, Z.; Liu, R.; Zhao, Y.; Zhang, X.; Wu, M.; Qin, Y.; Sun, C.; Yao, W.; Cao, Z.; Ajayan, P. M.; Chee, M. O. L.; Dong, P.; Li, Z.; Shen, J.; Ye, M. Liquid Metal-tailored Gluten Network for Protein-based E-skin. *Nat. Commun.* **2022**, *13*, 1206.

(18) Barber, J. R.; Yoon, H. J.; Bowers, C. M.; Thuo, M. M.; Breiten, B.; Gooding, D. M.; Whitesides, G. M. Influence of Environment on the Measurement of Rates of Charge Transport across AgTS/SAM//Ga₂O₃/EGaIn Junctions. *Chem. Mater.* **2014**, *26*, 3938–3947.

(19) Simeone, F. C.; Yoon, H. J.; Thuo, M. M.; Barber, J. R.; Smith, B.; Whitesides, G. M. Defining the Value of Injection Current and Effective Electrical Contact Area for EGaIn-Based Molecular Tunneling Junctions. *J. Am. Chem. Soc.* **2013**, *135*, 18131–18144.

(20) Ren, L.; Zhuang, J.; Casillas, G.; Feng, H.; Liu, Y.; Xu, X.; Liu, Y.; Chen, J.; Du, Y.; Jiang, L.; Dou, S. X. Nanodroplets for Stretchable Superconducting Circuits. *Adv. Funct. Mater.* **2016**, *26*, 8111–8118.

(21) Peng, H.; Xin, Y.; Xu, J.; Liu, H.; Zhang, J. Ultra-stretchable Hydrogels with Reactive Liquid Metals As Asymmetric Force-sensors. *Mater. Horiz.* **2019**, *6*, 618–625.

(22) Yamaguchi, A.; Mashima, Y.; Iyoda, T. Reversible Size Control of Liquid-Metal Nanoparticles under Ultrasonication. *Angew. Chem., Int. Ed.* **2015**, *54*, 12809.

(23) Wang, M.; Feng, X.; Wang, X.; Hu, S.; Zhang, C.; Qi, H. Facile Gelation of A Fully Polymeric Conductive Hydrogel Activated by Liquid Metal Nanoparticles. *J. Mater. Chem. A* **2021**, *9*, 24539–24547.

(24) Zhao, Q.; Jamal, R.; Zhang, L.; Wang, M.; Abdiryim, T. The Structure and Properties of PEDOT Synthesized by Template-free Solution Method. *Nanoscale Res. Lett.* **2014**, *9*, 557.

(25) Lee, J.; Choi, W. Surface Modification of Sulfur Cathodes with PEDOT:PSS Conducting Polymer in Lithium-Sulfur Batteries. *J. Electrochem. Soc.* **2015**, *162*, A935–A939.

(26) Lang, U.; Müller, E.; Naujoks, N.; Dual, J. Microscopical Investigations of PEDOT:PSS Thin Films. *Adv. Funct. Mater.* **2009**, *19*, 1215–1220.

(27) Ouyang, J.; Xu, Q.; Chu, C.-W.; Yang, Y.; Li, G.; Shinar, J. On the Mechanism of Conductivity Enhancement in Poly(3,4-ethylenedioxythiophene):poly(styrene sulfonate) Film through Solvent Treatment. *Polymer* **2004**, *45*, 8443–8450.

(28) Zhou, J.; Lubineau, G. Improving Electrical Conductivity in Polycarbonate Nanocomposites Using Highly Conductive PEDOT/PSS Coated MWCNTs. *ACS Appl. Mater. Interfaces* **2013**, *5*, 6189–6200.

(29) Kara, M. O. P.; Frey, M. W. Effects of Solvents on the Morphology and Conductivity of Poly(3,4-ethylenedioxythiophene):Poly(styrenesulfonate) Nanofibers. *J. Appl. Polym. Sci.* **2014**, *131*, 40305.

(30) Han, M. G.; Foulger, S. H. Facile Synthesis of Poly(3,4-ethylenedioxythiophene) Nanofibers from an Aqueous Surfactant Solution. *Small* **2006**, *2*, 1164–1169.

(31) Hu, X.; Chen, G.; Wang, X.; Wang, H. Tuning Thermoelectric Performance by Nanostructure Evolution of a Conducting Polymer. *J. Mater. Chem. A* **2015**, *3*, 20896–20902.

(32) Aasmundtveit, K. E.; Samuelsen, E. J.; Pettersson, L. A. A.; Inganäs, O.; Johansson, T.; Feidenhans'l, R. Structure of Thin Films of Poly(3,4-ethylenedioxythiophene). *Synth. Met.* **1999**, *101*, S61–S64.

(33) Kim, N.; Lee, B. H.; Choi, D.; Kim, G.; Kim, H.; Kim, J.-R.; Lee, J.; Kahng, Y. H.; Lee, K. Role of Interchain Coupling in the Metallic State of Conducting Polymers. *Phys. Rev. Lett.* **2012**, *109*, 106405.

(34) Xia, Y.; Ouyang, J. Salt-Induced Charge Screening and Significant Conductivity Enhancement of Conducting Poly(3,4-ethylenedioxythiophene):Poly(styrenesulfonate). *Macromolecules* **2009**, *42*, 4141–4147.

(35) Farah, A. A.; Rutledge, S. A.; Schaarschmidt, A.; Lai, R.; Freedman, J. P.; Helmy, A. S. Conductivity Enhancement of Poly(3,4-ethylenedioxythiophene)-poly(styrenesulfonate) Films Post-spincoating. *J. Appl. Phys.* **2012**, *112*, 113709.

(36) Li, Y.; Ren, G.; Zhang, Z.; Teng, C.; Wu, Y.; Lu, X.; Zhu, Y.; Jiang, L. A Strong and Highly Flexible Aramid Nanofibers/PEDOT:PSS Film for All-solid-state Supercapacitors with Superior Cycling Stability. *J. Mater. Chem. A* **2016**, *4*, 17324–17332.

(37) Xia, Y.; Sun, K.; Ouyang, J. Solution-Processed Metallic Conducting Polymer Films As Transparent Electrode of Optoelectronic Devices. *Adv. Mater.* **2012**, *24*, 2436–2440.

(38) Xia, Y.; Sun, K.; Ouyang, J. Highly Conductive Poly(3,4-ethylenedioxythiophene):poly(styrene sulfonate) Films Treated with an Amphiphilic Fluoro Compound As the Transparent Electrode of Polymer Solar Cells. *Energy Environ. Sci.* **2012**, *5*, 5325–5332.

(39) Lee, W.; Lee, S.; Kim, H.; Kim, Y. Organic Thermoelectric Devices with PEDOT:PSS/ZnO Hybrid Composites. *Chem. Eng. J.* **2021**, *415*, 128935.

(40) Creighton, M. A.; Yuen, M. C.; Susner, M. A.; Farrell, Z.; Maruyama, B.; Tabor, C. E. Oxidation of Gallium-based Liquid Metal Alloys by Water. *Langmuir* **2020**, *36*, 12933–12941.

(41) Khan, M. R.; Trlica, C.; So, J.-H.; Valeri, M.; Dickey, M. D. Influence of Water on the Interfacial Behavior of Gallium Liquid Metal Alloys. *ACS Appl. Mater. Interfaces* **2014**, *6*, 22467–22473.

(42) Hohman, J. N.; Kim, M.; Wadsworth, G. A.; Bednar, H. R.; Jiang, J.; LeThai, M. A.; Weiss, P. S. Directing Substrate Morphology via Self-Assembly: Ligand-Mediated Scission of Gallium-Indium Microspheres to the Nanoscale. *Nano Lett.* **2011**, *11*, 5104–5110.

(43) Farrell, Z. J.; Tabor, C. Control of Gallium Oxide Growth on Liquid Metal Eutectic Gallium/Indium Nanoparticles via Thiolation. *Langmuir* **2018**, *34*, 234–240.

(44) Huang, X.; Xu, T.; Shen, A.; Davis, T. P.; Qiao, R.; Tang, S.-Y. Engineering Polymers via Understanding the Effect of Anchoring Groups for Highly Stable Liquid Metal Nanoparticles. *ACS Appl. Nano Mater.* **2022**, *5*, 5959–5971.

(45) Alemu Mengistie, D.; Wang, P.-C.; Chu, C.-W. Effect of Molecular Weight of Additives on the Conductivity of PEDOT:PSS and Efficiency for ITO-free Organic Solar Cells. *J. Mater. Chem. A* **2013**, *1*, 9907–9915.

(46) Zhang, P.; Wang, Q.; Guo, R.; Zhang, M.; Wang, S.; Lu, C.; Xue, M.; Fan, J.; He, Z.; Rao, W. Self-assembled Ultrathin Film of CNC/PVA-Liquid Metal Composite As a Multifunctional Janus material. *Mater. Horiz.* **2019**, *6*, 1643–1653.

(47) Li, X.; Li, M.; Xu, J.; You, J.; Yang, Z.; Li, C. Evaporation-induced Sintering of Liquid Metal Droplets with Biological Nanofibrils for Flexible Conductivity and Responsive Actuation. *Nat. Commun.* **2019**, *10*, 3514.

(48) Sobhani, Z.; Al Amin, M.; Naidu, R.; Megharaj, M.; Fang, C. Identification and Visualisation of Microplastics by Raman Mapping. *Anal. Chim. Acta* **2019**, *1077*, 191–199.

(49) Ryan, J. D.; Mengistie, D. A.; Gabrielsson, R.; Lund, A.; Muller, C. Machine-Washable PEDOT:PSS Dyed Silk Yarns for Electronic Textiles. *ACS Appl. Mater. Interfaces* **2017**, *9*, 9045–9050.

(50) Pan, H.; Zhang, Y.; Shao, H.; Hu, X.; Li, X.; Tian, F.; Wang, J. Nanoconfined Crystallites Toughen Artificial Silk. *J. Mater. Chem. B* **2014**, *2*, 1408–1414.

(51) Soh, S.; Liu, H.; Cademartiri, R.; Yoon, H. J.; Whitesides, G. M. Charging of Multiple Interacting Particles by Contact Electrification. *J. Am. Chem. Soc.* **2014**, *136*, 13348–13354.

(52) Thomas, S. W., III; Vella, S. J.; Kaufman, G. K.; Whitesides, G. M. Patterns of Electrostatic Charge and Discharge in Contact Electrification. *Angew. Chem., Int. Ed.* **2008**, *47*, 6654–6656.

(53) Xu, C.; Zi, Y.; Wang, A. C.; Zou, H.; Dai, Y.; He, X.; Wang, P.; Wang, Y.-C.; Feng, P.; Li, D.; Wang, Z. L. On the Electron-Transfer Mechanism in the Contact-Electrification Effect. *Adv. Mater.* **2018**, *30*, 1706790.